Journal of Systems Engineering and Electronics
Vol. 32, No. 6, December 2021, pp.1284 – 1303

InSAR measurements of surface deformation over permafrost on Fenghuoshan Mountains section, Qinghai-Tibet Plateau

YANG Honglei[1,*], JIANG Qiao[2], HAN Jianfeng[1], KANG Ki-Yeob[3], and PENG Junhuan[1]

1. School of Land Science and Technology, China University of Geosciences (Beijing), Beijing 100083, China; 2. Central Southern China Electric Power Design Institute Co., Ltd, China Power Engineering Consulting Group Corporation, Wuhan 430071, China; 3. Australasian Joint Research Centre for Building Information Modelling, School of Built Environment, Curtin University, Perth WA 6845, Australia

Abstract: The permafrost development in the Qinghai-Tibet Engineering Corridor (QTEC) is affected by natural environment changes and human engineering activities. Human engineering activities may damage the permafrost growing environment, which in turn impact these engineering activities. Thus high spatial-temporal resolution monitoring over the QTEC in the permafrost region is very necessary. This paper presents a method for monitoring the frozen soil area using the intermittent coherence-based small baseline subset (ICSBAS). The method can improve the point density of the results and enhance the interpretability of deformation results by identifying the discontinuous coherent points according to the coherent value of time series. Using the periodic function that models the seasonal variation of permafrost, we separate the long wavelength atmospheric delay and establish an estimation model for the frozen soil deformation. Doing this can raise the monitoring accuracy and improve the understanding of the surface deformation of the frozen soil. In this study, we process 21 PALSAR data acquired by the Alos satellite with the proposed ICSBAS technique. The results show that the frozen soil far from the QTR in the study area experiences frost heave and thaw settlement (4.7 cm to 8.4 cm) alternatively, while the maximum settlement along the QTR reaches 12 cm. The interferomatric syntnetic aperture radar (InSAR)-derived results are validated using the ground leveling data nearby the Beiluhe basin. The validation results show the InSAR results have good consistency with the leveling data in displacement rates as well as time series. We also find that the deformation in the permafrost area is correlated with temperature, human activities and topography. Based on the interfering degree of human engineering activities on the permafrost environment, we divide the QTEC along the Qinghai-Tibet Railway into engineering damage zone, transition zone and natural permafrost.

Keywords: permafrost, Qinghai-Tibet Plateau, small baseline subset interferomatric syntnetic aperture radar (SBAS-InSAR), deformation model.

DOI: 10.23919/JSEE.2021.000109

1. Introduction

The Qinghai-Tibet Plateau (QTP), with an average elevation of higher than 4 000 m, developed the highest and largest permafrost area in the world [1]. Global warming, melting and degradation of permafrost lead to significant changes to surface water balance, ecosystems, surface hydrology, carbon cycle processes and geomorphic processes, which induce surface subsidence that in turn impacts the stability of frozen soil structures [2]. The Qinghai-Tibet Engineering Corridor (QTEC), accommodating a number of major linear projects, such as railways, highways, oil pipelines and communication cables, has about 550 km passing through the permafrost region. Therefore, these projects are challenged by the permafrost changes. Therefore, large-scale deformation monitoring over permafrost areas is of great significance for ensuring the stability of projects in the QTEC, and the sustainable economic and social development of the plateau.

Several methods have been used to determine seasonal and long-term changes of the active layer thickness (ALT), such as the borehole method [3] leveling surveying [4], global positioning system (GPS) [5] and the ground-penetrating radar (GPR) [6,7]. However, these methods have strict topographical and environmental conditions, and require expensive and non-portable equipment. Furthermore, they can only monitor a few points or small regions. The interferometric synthetic aperture radar (InSAR) technology can map land subsidence over extensive areas with high spatial resolution

Manuscript received March 10, 2021.
*Corresponding author.
This work was supported by the National Natural Science Foundation of China (42174026), and the National Key Research and Development Program of China (2021YFE011004).

and precision under all weathers [8]. Particularly, the differential InSAR (D-InSAR) has been recently utilized to monitor the surface deformation relating to the freezing and thawing process of permafrost [9−14]. However, D-InSAR can only measure single deformations rather than deformation time series, and is vulnerable to spatial-temporal decorrelation and atmospheric delays. Multi-temporal SAR interferometry (MT-InSAR) [15,16] can overcome these problems by analyzing multiple SAR images over the same area, and can derive high accuracy deformation time series.

Traditional time-series InSAR technologies only reverse deformations in high coherent areas (e.g., bare rock and large artificial facilities), but not in low coherent areas (e.g., vegetation, snow cover, mire), which brings difficulties to deformation interpretation [17−25]. Therefore, this study attempts to improve the high coherence point selection method, and to perform time-series analysis on the differential interference phase of intermittent high coherence points. By doing so, the point density of the monitoring results can be improved, and the deformation of the whole study area can be revealed completely.

The time-series InSAR describes the surface deformation using a linear model [18], and restores the nonlinear deformation from un-modeled residuals. However, using the linear deformation model could result in large residual phases (π) and biased deformation estimations, when the frozen soil deformation is significantly nonlinear [26]. Therefore, an appropriate mathematical model is needed to accurately estimate the surface deformation and reduce the deviation between the theoretical model and the real ground deformation. A couple of models have been proposed for this, such as the periodic model considering seasonal uplift (frost heave) and subsidence (thaw settlement) [13], the InSAR deformation model considering the ground surface temperature and the number of thaw days [17,20] and the deformation model focusing on climatic factors [25]. Wang et al. presented a seasonal deformation model based on the simplified Stefan equation which has been adopted to measure the seasonal displacement [27]. Chen et al. combined a both cut-edge algorithms for identification of radar distributed scatters and eigenvalue-decomposition-based optimization to improve the spatial and temporal resolutions of deformation measurements [28]. Huang et al. improved the traditional small baseline subset InSAR (SBAS-InSAR) method by adding the error correction and noise reduction [29]. However, none of these models can approximate the influences of all factors on the deformation, and none single model can model the whole study area. Therefore, we propose to separate the atmospheric delay phase using a periodic function, and establish a set of linear equations of the deformation velocities and the digital evaluation model (DEM) height correction for each selected high coherent point. Moreover, a set of weighted constraints on the fast surface changes are added to the designed matrix.

To address the above issues, we choose 21 ALOS PALSAR images (acquired from 17 June 2007 to 28 October 2010) covering the Fenghuoshan Mountains to monitor the deformation of the frozen soil, using the intermittent coherence-based SBAS-InSAR. Different from traditional point or linear deformation analyses, this study analyzes the correlation between the deformation and temperature in two dimensions. Based on this correlation, we detect the influence of human activities and topography on the frozen soil. According to the influence of human engineering activities on the permafrost, the QTEC along the Qinghai-Tibet Railway (QTR) is divided into the damaged zone, transition zone and natural permafrost.

This paper is organized as follows: we introduce the climate, geological conditions and vegetation coverage of the study area, as well as the experiment data in Section 2. After summarizing the proposed algorithm and data processing in Section 3, we analyze the obtained results in Section 4. We then discuss the influences of human activities, slopes and aspects on the frozen soil deformation based on the correlation coefficient of time series deformation and temperature in Section 5. Some conclusions are drawn finally.

2. Study site and data

2.1 Study site

We select the Fenghuoshan Mountains as the study area, located in the north of the Tanggula Mountains and the south of Hoh Xil (see Fig. 1). It extends an area about 420 km^2 between 34°36′N to 34°53′N and 92°44′E to 92°58′E. In Fig. 1(a), the part in the black rectangle is the study area. The QTEC passing through this area (see Fig. 1(b)) accommodates many great linear projects, including the QTR, the Qinghai-Tibet Highway (QTH) and the Golmud-Lhasa oil pipeline. In Fig. 1(c), t1 refers to a point in the frozen soil area, t2 refers to a point along the QTR, and t3 refers to a point along the ridge. The black line indicates the Tibetan engineering corridor (dense regions of human activity). The topography of the study area is dominated by high plains, hills and mountains. The Fenghuoshan Mountains has an arid continental climate. In recent years, the temperature (air temperature

and ground temperature) and precipitation there both increased [30]. The average monthly rainfall in the region is about 100 mm. The rain concentrates in July to September, and in other months, the precipitation is in forms of snow or hail. The mean annual air temperature there is about −3.8℃, with the highest temperature 23℃ in July or August, and the lowest temperature −38℃ in January or February.

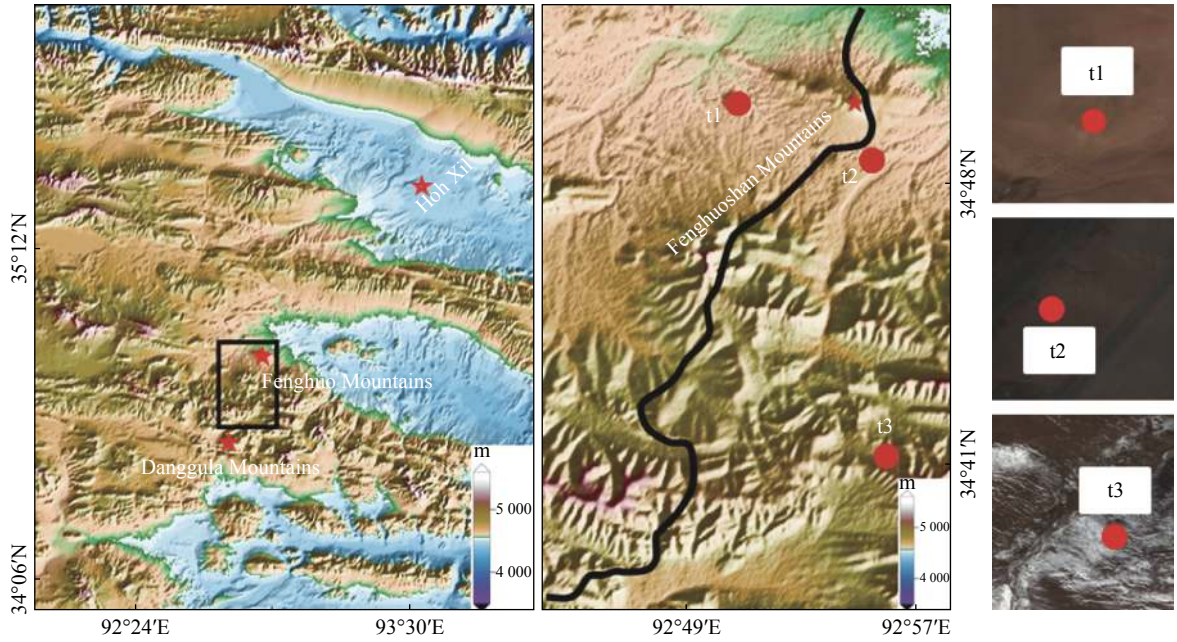

(a) Topographic map of the Qinghai-Tibet Plateau (b) Topographic map of the study area (c) Three typical points

Fig. 1 The map of the study area

The study area has a diverse vegetation distribution. Areas higher than 5 100 m are alpine permafrost desert, with sparse vegetation. In the valley beach and smooth hillside above 4 900 m, the vegetation coverage is patchy or flaky. A few mountains with slopes of 15° to 25° have a vegetation coverage less than 50%. However, on smooth slopes toward the sun, the vegetation coverage is up to 80%. The study area has a large area of permafrost. The frozen soil is 50−120 m in thickness with the active layer of 0.8−2.5 m in thickness. The active layer has seasonal frost heave and thaw, resulting in frost mounds and thaw depression.

2.2 Data

The 21 ALOS PALSAR images (Table 1), ranging from January 2007 to October 2010, were acquired with the ascending orbit with a look angle of 38°. The polarization is HH and the band is L-band. The pixel spacing is 4.680 m and 3.149 m in the range and azimuth directions, respectively. We also use the shuttle radar topography mission (SRTM) 1-arcsecond DEM (about 30 m spacing) provided by NASA to simulate topographic phases subtracted from the original interferograms. We verify the monitoring results by the second-class leveling monitoring results (from January 2007 to December 2010 with an interval of one month).

Table 1 Basic parameters of SAR images

Number	Sensor	Acquisition time (year-month-day)	Perpendicular baseline/m
1	PALSAR	2007-01-17	0
2	PALSAR	2007-03-04	1 839.02
3	PALSAR	2007-07-20	2 527.09
4	PALSAR	2007-09-04	2 708.44
5	PALSAR	2007-10-20	2 925.88
6	PALSAR	2008-01-20	3 484.94
7	PALSAR	2008-03-06	4 067.51
8	PALSAR	2008-04-21	4 518.52
9	PALSAR	2008-06-06	4 462.98
10	PALSAR	2008-07-22	1 516.82
11	PALSAR	2008-09-06	−663.26
12	PALSAR	2008-10-22	−91.87
13	PALSAR	2009-01-22	498.06
14	PALSAR	2009-03-09	904.87
15	PALSAR	2009-07-25	1 131.38
16	PALSAR	2009-09-09	1 641.92
17	PALSAR	2009-10-25	1 898.51
18	PALSAR	2010-01-25	2 612.77
19	PALSAR	2010-07-28	3 499.58
20	PALSAR	2010-09-12	3 551.67
21	PALSAR	2010-10-28	3 968.39

To explain the frozen soil deformation, we also employ the MOD11A1 and MYD11A1 products of Terra Satellite and Aqua Satellite, respectively. These images also span from January 17, 2007 to October 28, 2010, with the time resolution of one day, the spatial resolution of 1 km and the projection mode as pseudo cylindrical equal area projection. We use the night temperature data, because the SAR data were acquired at night. As shown in Fig. 2, the average surface temperature has a continuous growth from 2007 to 2010. (The time is consistent with ALOS data acquisition time)

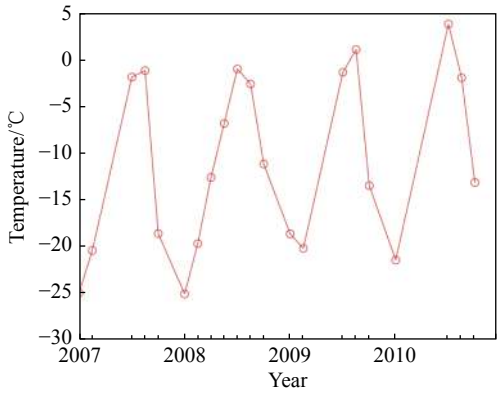

Fig. 2 Average night temperature between 2007 and 2010

3. Data processing and methodology

3.1 Intermittent coherent SBAS technique

Assuming M SAR images over one region are acquired at moment t $(t_1, t_2, \cdots, t_M)$ and are registered in the same coordinate system, N interferometric pairs are generated within certain temporal and spatial baseline thresholds. N [16] is

$$\frac{M}{2} \leqslant N \leqslant \frac{M(M-1)}{2}. \tag{1}$$

3.1.1 High coherence point selection

Filter and unwrap the generated differential interferogram. Then we select high coherent points from the unwrapped differential interferogram using the coherence information. Traditional SBAS methods generally select high coherent points, such as point G_1 in Fig. 3.

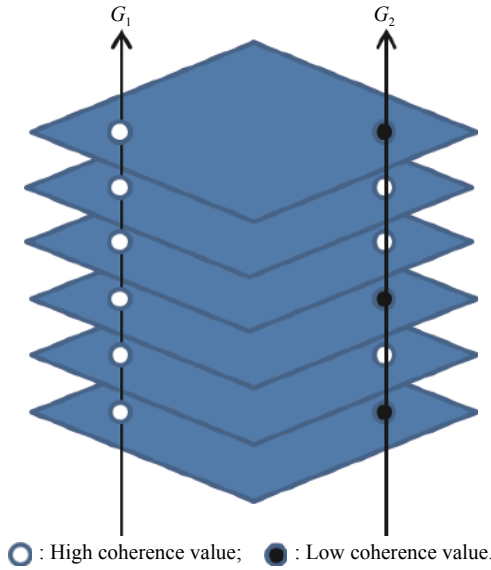

Fig. 3 Schematic of the high coherence point and intermittent high coherence point

We propose a new SBAS technique, using points with intermittent coherence in the time series (point G_2) as a complementary to high coherence points. The method of selecting intermittent coherence points is based on two criteria:

(i) The threshold for the average coherence across all interferograms is set to 0.25;

(ii) Only those points showing coherence higher than 0.25 are kept for the subsequent processing steps, the number of coherent points for those pixels is based on

$$\frac{2}{3}N \leqslant n \leqslant N. \tag{2}$$

3.1.2 Establishing equations based on coherent points

Assuming that the jth unwrapped differential interferogram is computed from SAR images at moment t_m^j (master image) and t_s^j (slave image), the phase value of the high coherence point is

$$\delta\varphi_j(x,r) = \varphi(t_s^j,x,r) - \varphi(t_m^j,x,r) = \frac{4\pi}{\lambda}\left[d(t_s^j,x,r) - d(t_m^j,x,r)\right] + \frac{4\pi}{\lambda}\frac{B_{\perp j}}{R_j \sin\theta_j}\Delta z(x,r) + \varphi_j^{atm}(x,r) + \Delta n_i(x,r) \tag{3}$$

where λ is the radar wavelength (23.6 cm for L-band data), $d(t_s^j,x,r)$ and $d(t_m^j,x,r)$ are the line-of-sight (LOS) deformation at moments t_m^j and t_s^j accumulated from t_1 (the reference time). $B_{\perp j}$ represents the perpendicular baseline of the jth differential interferogram. $\Delta z(x,r)$ and $\varphi_j^{atm}(x,r)$ are the DEM error and the atmospheric delay, respectively. $\Delta n_i(x,r)$ is the noise phase caused by the loss of correlation. R_j and θ_j are the slant range distance and the incident angle of the jth differential interferogram.

The low-frequency deformation of the permafrost consists of linear subsidence and seasonal periodic deformation [13], which can be expressed as [31,32]

$$d(t,x,r) = a_1(x,r)t + a_2(x,r)\cos\left(\frac{2\pi}{T}t\right) \tag{4}$$

where t is the deformation cumulative time, $a_1(x,r)$ is the linear deformation rate and $a_2(x,r)$ is a periodic model parameter. T is the seasonal deformation cycle, generally one year. Thus (3) can be rewritten as

$$\delta\varphi_j(x,r) = \varphi(t_s^j,x,r) - \varphi(t_m^j,x,r) = a_1(x,r)\left(t_s^j - t_m^j\right) + a_2(x,r)\left(\cos\left(\frac{2\pi}{T}t_s^j\right) - \cos\left(\frac{2\pi}{T}t_m^j\right)\right) + \frac{4\pi}{\lambda}\frac{B_{\perp j}}{R_j\sin\theta_j}\Delta z(x,r) + \Delta\varphi_j^{res}(x,r) \tag{5}$$

where $\Delta\varphi_j^{res}(x,r)$ is the residual phase of the jth differential interferogram. For the transformation of (5), the phase of all the differential interferograms can be expressed as

$$\delta\boldsymbol{\varphi}(x,r) = \boldsymbol{A}\boldsymbol{\beta}(x,r) + \Delta\boldsymbol{\varphi}^{res}(x,r) \tag{6}$$

where $\boldsymbol{\beta}(x,r)$ is the unknown vector of pixel (x,r), $\delta\boldsymbol{\varphi}(x,r)$ is the phase vector pixel(x,r) in all differential interferograms, and $\boldsymbol{A}$ is the coefficient matrix.

$$\begin{bmatrix} \delta\varphi_1(x,r) \\ \delta\varphi_2(x,r) \\ \vdots \\ \delta\varphi_j(x,r) \\ \vdots \\ \delta\varphi_N(x,r) \end{bmatrix} = \begin{bmatrix} t_s^1 - t_m^1 & \cos\left(\frac{2\pi}{T}t_s^1\right) - \cos\left(\frac{2\pi}{T}t_m^1\right) & \frac{4\pi}{\lambda}\frac{B_{\perp 1}}{R_1\sin\theta_1} \\ t_s^2 - t_m^2 & \cos\left(\frac{2\pi}{T}t_s^2\right) - \cos\left(\frac{2\pi}{T}t_m^2\right) & \frac{4\pi}{\lambda}\frac{B_{\perp 2}}{R_2\sin\theta_2} \\ \vdots & \vdots & \vdots \\ t_s^j - t_m^j & \cos\left(\frac{2\pi}{T}t_s^j\right) - \cos\left(\frac{2\pi}{T}t_m^j\right) & \frac{4\pi}{\lambda}\frac{B_{\perp j}}{R_j\sin\theta_j} \\ \vdots & \vdots & \vdots \\ t_s^N - t_m^N & \cos\left(\frac{2\pi}{T}t_s^N\right) - \cos\left(\frac{2\pi}{T}t_m^N\right) & \frac{4\pi}{\lambda}\frac{B_{\perp N}}{R_N\sin\theta_N} \end{bmatrix} \begin{bmatrix} a_1(x,r) \\ a_2(x,r) \\ \Delta z(x,r) \end{bmatrix} + \begin{bmatrix} \Delta\varphi_1^{res}(x,r) \\ \Delta\varphi_2^{res}(x,r) \\ \vdots \\ \Delta\varphi_j^{res}(x,r) \\ \vdots \\ \Delta\varphi_N^{res}(x,r) \end{bmatrix} \tag{7}$$

The least square solution of parameters of each pixel is

$$\hat{\boldsymbol{\beta}} = \left(\boldsymbol{A}^{\mathrm{T}}\boldsymbol{A}\right)^{-1}\boldsymbol{A}^{\mathrm{T}}\delta\boldsymbol{\varphi}, \tag{8}$$

$$\delta\hat{\boldsymbol{\varphi}} = \boldsymbol{A}\hat{\boldsymbol{\beta}}, \tag{9}$$

$$\Delta\hat{\boldsymbol{\varphi}}^{res} = \delta\boldsymbol{\varphi} - \delta\hat{\boldsymbol{\varphi}}, \tag{10}$$

where $\Delta\hat{\boldsymbol{\varphi}}^{res}$ is the phase of the differential interferograms after the linear and periodical deformation subjection and the elevation correction.

3.1.3 Inversion of the deformation time series

The differential interferograms contain high frequency deformations, atmospheric delays and noises. The atmospheric delay has high spatial correlation and poor temporal correlation, but the high frequency deformation is highly correlated both in spatial and temporal domains. Noise shows poor correlation in both the spatial and temporal domain. Thus the atmospheric delay phase could be separated using the large-scale atmospheric delay filtering [33]. After the filtering, the differential interferogram only has deformation, elevation error and noise.

$$\delta\bar{\varphi}_j(x,r) = \frac{4\pi}{\lambda}\left[d(t_s^j,x,r) - d(t_m^j,x,r)\right] + \frac{4\pi}{\lambda}\frac{B_{\perp j}}{R_j\sin\theta_j}\Delta z(x,r) + \Delta n_j^{\bullet}(x,r) + \Delta n_j^{\bullet}(x,r) \tag{11}$$

where $\delta\bar{\varphi}_j(x,r)$ is the interferogram phase for removing the atmospheric delay, and $\Delta n_j^{\bullet}(x,r)$ consists of noise and atmospheric residuals.

Solving the deformation with (11) will result in great jumps in time, so we solve the phase velocity instead. The phase velocity can be expressed as a vector:

$$\boldsymbol{v}_{\mathrm{phase}}^{\mathrm{T}} = [v_1, v_2, \cdots, v_{i-1}, v_i, \cdots, v_{M-1}], \quad v_i = \frac{\phi_{i+1} - \phi_i}{t_{i+1} - t_i}. \tag{12}$$

We assume that the phase velocities at adjacent moments meet the following constraint:

$$v_{i+1}(x,r) - 2v_i(x,r) + v_{i-1}(x,r) \sim \mathrm{N}(0, \sigma_v^2 = w^{-2}) \tag{13}$$

which can be represented by a virtual observation equation($l_i(x,r)=0$):

$$l_i(x,r)=v_{i+1}(x,r)-2v_i(x,r)+v_{i-1}(x,r)+n_{l_i},$$
$$n_{l_i}\sim \mathrm{N}(0,\sigma_v^2=w^{-2}) \tag{14}$$

where the weighting factor w varies from 0 (no smoothing) to a large value [34]. The non-linearity and coherence of the deformation should be taken into account when we tune the factor. The frozen soil has obvious nonlinear deformation, so the prior value of w is relatively small. As previously mentioned, the moments of the master and slave images of the jth differential interferogram are t_m^j and t_s^j ($t_m^j,t_{m+1}^j,\cdots,t_{s-1}^j,t_s^j$), so (12) can be rewritten as

$$\delta\bar{\varphi}_j(x,r)=\sum_{i=m+1}^{s}\left(t_i^j-t_{i-1}^j\right)v_i(x,r)+\frac{4\pi}{\lambda}\frac{B_{\perp j}}{R_j\sin\theta_j}\Delta z(x,r)+n_j^{\bullet}(x,r),\quad j=1,\cdots,N. \tag{15}$$

Jointly analyze (14) and (15) by the following matrix:

$$\boldsymbol{L}=\boldsymbol{B}\Psi+\Delta\boldsymbol{n}^{\bullet} \tag{16}$$

where $\boldsymbol{L}=\begin{bmatrix}\delta\bar{\varphi}\\ l\end{bmatrix}$ is a vector matrix of the phase value of all differential interferogram without atmosphere delay and virtual observation value; $\boldsymbol{\Psi}$ is the vector matrix of unknown parameters; $\boldsymbol{B}$ is the coefficient matrix; $\Delta\boldsymbol{n}^{\bullet}$ is the noise and the residual phase of the atmosphere and elevation. Assuming there are six SAR images and their corresponding interferogram pairs, and with the weight of $\delta\bar{\varphi}_j(x,r)$ being 1, the observation equation is

$$\boldsymbol{L}=\begin{bmatrix}\delta\bar{\varphi}_1\\ \delta\bar{\varphi}_2\\ \delta\bar{\varphi}_3\\ \delta\bar{\varphi}_4\\ \delta\bar{\varphi}_5\\ \delta\bar{\varphi}_6\\ l_2\\ l_3\\ l_4\end{bmatrix}=\begin{bmatrix}t_2-t_1 & t_3-t_2 & 0 & 0 & 0 & \frac{4\pi}{\lambda}\frac{B_{\perp1}}{R_1\sin\theta_1}\\ 0 & t_3-t_2 & t_4-t_3 & t_5-t_4 & 0 & \frac{4\pi}{\lambda}\frac{B_{\perp2}}{R_2\sin\theta_2}\\ 0 & t_3-t_2 & t_4-t_3 & 0 & 0 & \frac{4\pi}{\lambda}\frac{B_{\perp3}}{R_3\sin\theta_3}\\ t_2-t_1 & t_3-t_2 & t_4-t_3 & 0 & 0 & \frac{4\pi}{\lambda}\frac{B_{\perp4}}{R_4\sin\theta_4}\\ 0 & 0 & 0 & t_5-t_4 & t_6-t_5 & \frac{4\pi}{\lambda}\frac{B_{\perp5}}{R_5\sin\theta_5}\\ 0 & 0 & t_4-t_3 & t_5-t_4 & t_6-t_5 & \frac{4\pi}{\lambda}\frac{B_{\perp6}}{R_6\sin\theta_6}\\ 1 & -2 & 1 & 0 & 0 & 0\\ 0 & 1 & -2 & 1 & 0 & 0\\ 0 & 0 & 1 & -2 & 1 & 0\end{bmatrix}\begin{bmatrix}v_1\\ v_2\\ v_3\\ v_4\\ v_5\\ \Delta z\end{bmatrix}+\begin{bmatrix}n_1^{\bullet}\\ n_2^{\bullet}\\ n_3^{\bullet}\\ n_4^{\bullet}\\ n_5^{\bullet}\\ n_6^{\bullet}\\ n_{l_2}\\ n_{l_3}\\ n_{l_4}\end{bmatrix}. \tag{17}$$

The weight matrix is

$$\boldsymbol{P}=\mathrm{diag}(1,1,1,1,1,1,w^2,w^2,w^2). \tag{18}$$

The least squares (LS) solution is

$$\boldsymbol{\Psi}=\left(\boldsymbol{B}^{\mathrm{T}}\boldsymbol{P}\boldsymbol{B}\right)^{-1}\boldsymbol{B}^{\mathrm{T}}\boldsymbol{P}\boldsymbol{L}. \tag{19}$$

We obtain the velocity v of adjacent time periods by (19). Integrating the velocity of each time period, we obtain the deformation of each time period, which is then multiplied by the transformation coefficient $\lambda/4\pi$ to generate the LOS deformation time series of the study area. This is the proposed intermittent coherence-based SBAS (ICSBAS), and the flowchart is shown in Fig. 4.

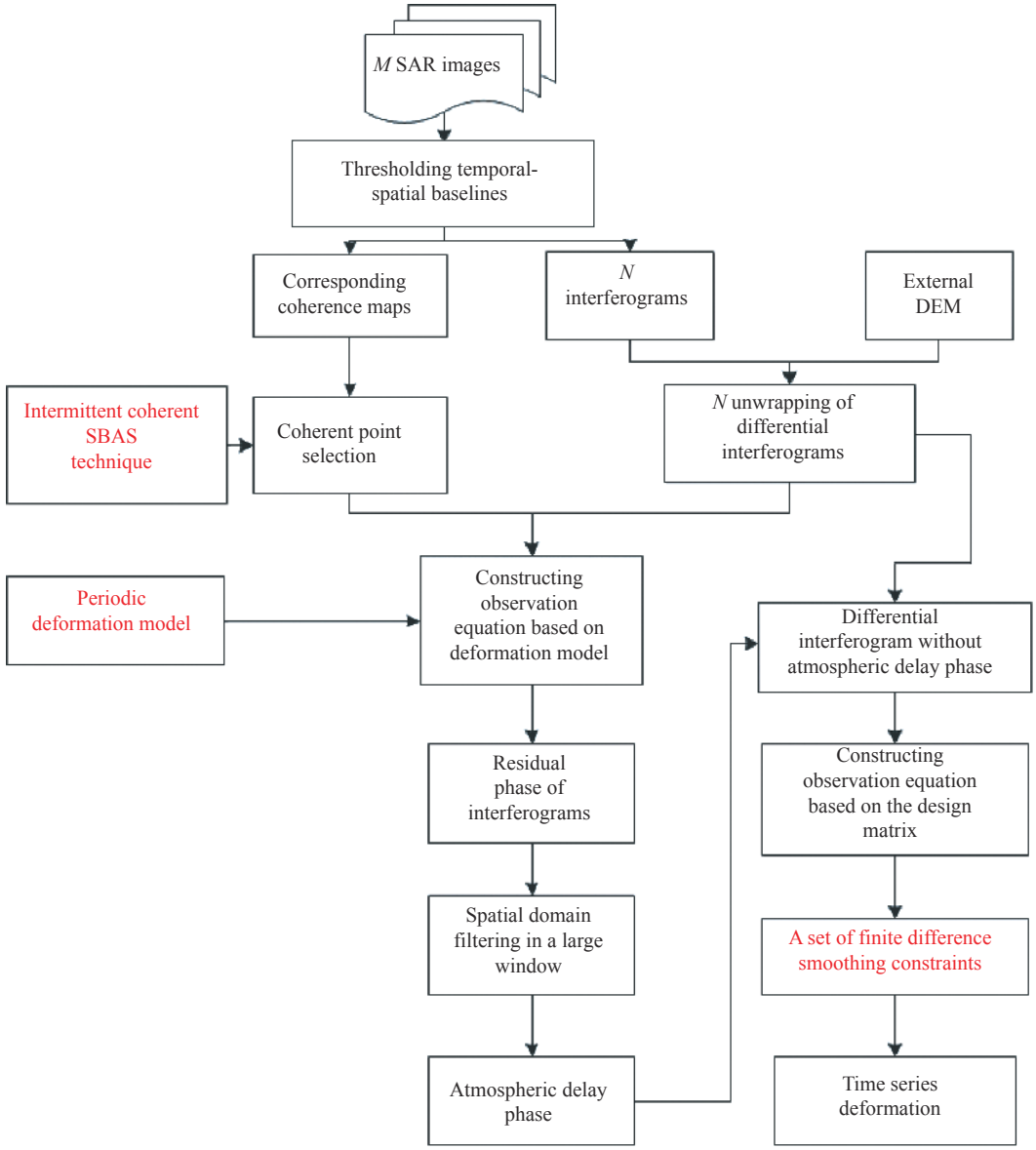

Fig. 4 Flowchart of the proposed ICSBAS technique

3.2 Data processing

We study the surface deformation of the permafrost in the Fenghuoshan Mountains by the proposed ICSBAS technique. Firstly, we generate 65 interferograms (Fig. 5) from the 21 ALOS images using the two-pass D-InSAR, with the perpendicular and temporal baselines smaller than 1 500 m and shorter than 366 days, respectively. Then, we simulate topographic phases using the SRTM 1-arcsecond DEM (about 30 m spacing) provided by NASA (http://gdex.cr.usgs.gov/gdex/), which is then subtracted from the original interferograms [35]. In addition, the multi-looking operation with two looks in the range and four looks in the azimuth direction is conducted to improve the differential interferograms and reduce the calculation load and noise. Then, the interferograms are filtered with the improved Goldstein filter [36] to further suppress the noise. After that, the minimum cost flow (MCF) method [37,38] is used to unwrap the interferometric phases of each interferogram. The reference point for phase unwrapping is set at a relatively stable and exposed bedrock. We select high coherence points by the proposed ICSBAS method and construct equations for each selected point. The low-pass (LP) surface deformation and residual differential interferogram, including the high-pass (HP) deformation, atmospheric delay and noise effects, are obtained by (9) and (10), respectively. Then the atmospheric delay is separated from the residual by a

large-scale atmospheric delay filtering method (consisting of multi-look, spatial filtering and spatial interpolation). After that, we get the deformation time series of the study area by (19).

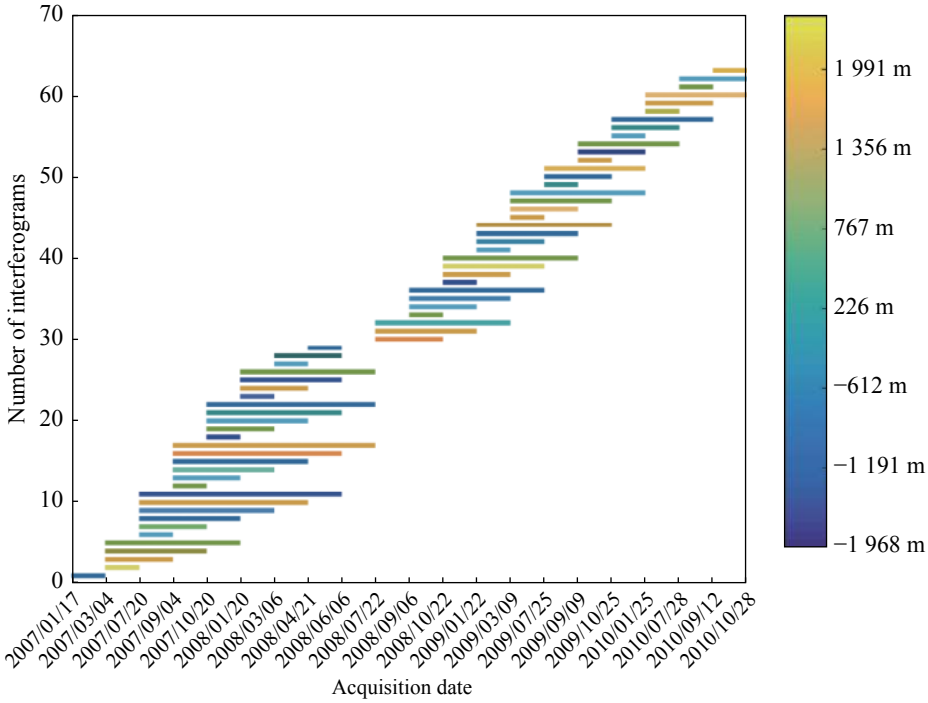

Fig. 5 Perpendicular spatial baselines and temporal intervals of the selected InSAR image pairs

In order to analyze the correlation between deformation and temperature, we process the moderate-resolution imaging spectroradiometer (MODIS) temperature data of the study area. Firstly, we convert the MODIS temperature product from the sin projection coordinates to the WGS-84 coordinates with the MODIS Reprojection Tool (MRT), and extract the nighttime surface temperatures for the experiment. After removing the outliers and NULL caused by clouds, the temperature data corresponding to the SAR time series are obtained and converted from the Fahrenheit temperature T to Celsius temperature t ($t = T - 273.15$) (see Fig. 6(a)). The obtained temperature data are registered and resampled with the deformation map to achieve the same resolution (Fig. 6(c)). Thus each pixel contains both the time series deformation and temperature. The correlation coefficient of deformation and temperature of each pixel is calculated, according to which the permafrost deformation and permafrost environment change are analyzed. In Fig. 6(a), the black box outlines the QTP.

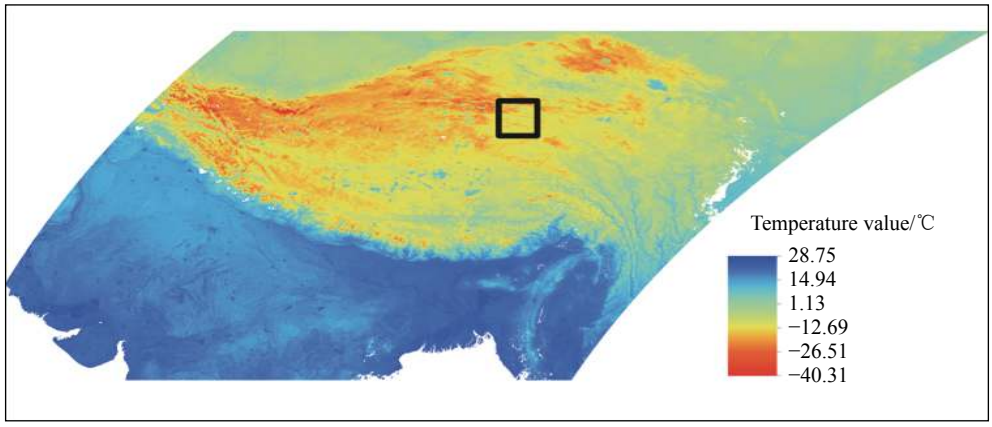

(a) MOD11A1 and MYD11A1 temperature data of Asia

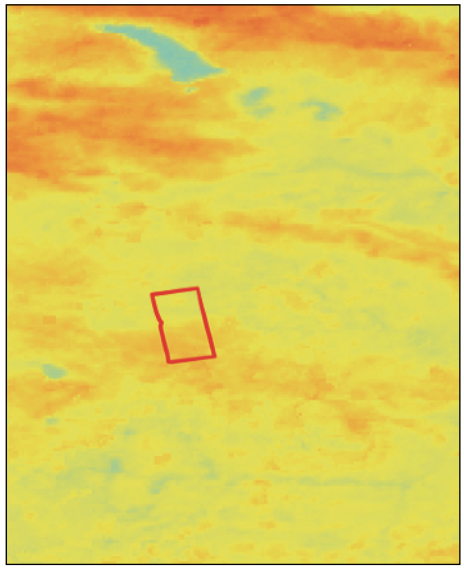

(b) Temperature data of the QTP, with the red polygon indicating the Fenghuoshan Mountains

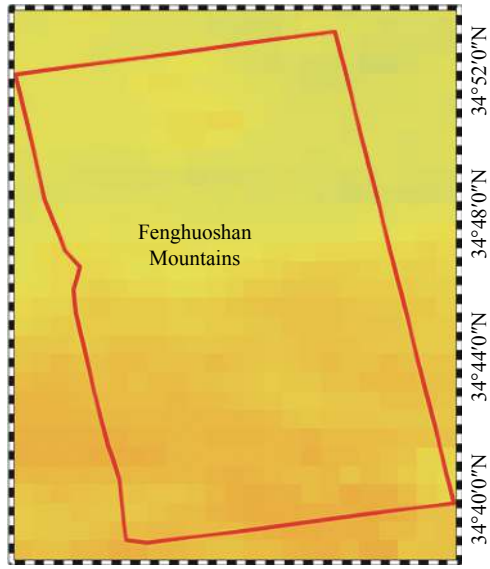

(c) The zoom in of the red polygon in (b)

Fig. 6 Temperature data

4. Results and analysis

4.1 Target point recognition based on intermittent high coherence

Traditional SBAS technologies can only monitor areas with high temporal coherence, such as exposed rocks and large artificial facilities, but cannot monitor vegetation with low coherence in the time domain. Thus the obtained deformation information is not complete, and brings difficulties to the result interpretation. Human activities, topography and temperature all have influences on the vegetation coverage, soil moisture and climate, which will change the physical features of the surface, thereby reducing the interferogram coherence and resulting in some pixels with intermittent coherence. These pixels may contain important deformation information in time series, but they are not considered by traditional SBAS technologies. As shown in Fig. 7(a), 122 771 high coherence points (CP) are selected by the traditional SBAS technology, accounting for 53.29% of the total pixels. The point density is relatively low, and some low coherent regions even have no point (see the green rectangular in Fig. 7(a)). Using the ICSBAS, we get 1 889 659 CPs, accounting for 82.36% of the total pixels (Fig. 7(b)). Thus, the proposed method significantly improves the CP density, especially in the low coherence region (see the green rectangular in Fig. 7(b)). Therefore, the ICSBAS obtains a more complete deformation field.

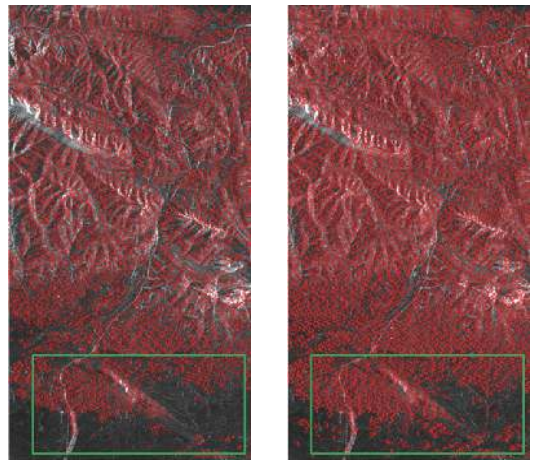

(a) Traditional SBAS (b) ICSBAS

Fig. 7 High CP selected by traditional SBAS and ICSBAS

4.2 Typical settlement area analysis

As Fig. 8(a) shows, the majority of permafrost regions (60% to 70%) are stable during the observation period, with a displacement velocity between −10 mm yr^{-1} and 10 mm yr^{-1}. Black rectangular boxes represent areas with significant deformations whose high-resolution optical images are shown in Fig. 9, and the black line presents the QTR. The regions adjacent to the QTR suffer more serious subsidence. And the subsidence increases from northeast to southwest with the rise of the elevation. Three regions have significant deformations (a, b, and c in Fig. 8(a)), so their high-resolution optical images from Google-Earth (Fig. 9) are used to investigate the causing factors. In mountainous areas, regions closer to the ridge

have greater subsidence (Fig. 9(c)). One reason is that the snow melting in the ridge reduces the snow elevation. In addition, the snow cover allows the heat to accumulate in the shallow surface, which leads to the active layer thawing and sinking. Also, serious weathering and erosion (Fig. 9(a) and Fig. 9(b)) break the slopes, resulting in persistent landslides and large surface subsidence. The estimated DEM errors (Fig. 8(b)) are between −6 m and 6 m in the major part of the study area, except some mountain areas (10 m). This is consistent with the accuracy of SRTM 1-arcsecond DEM provided by NASA (±10 m).

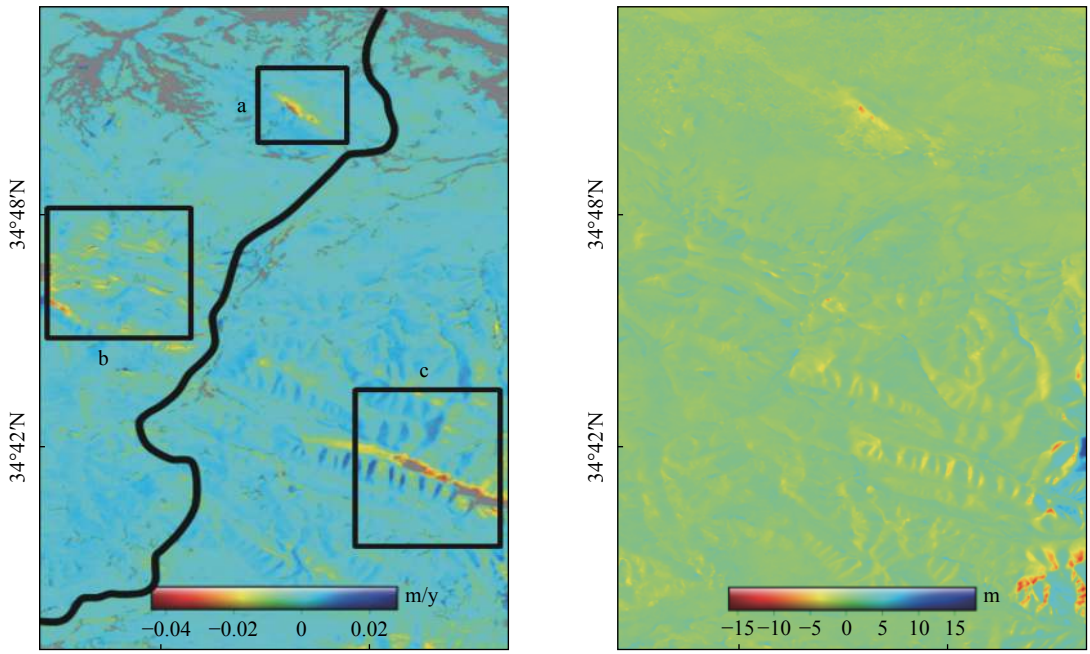

(a) The mean subsidence velocity (b) DEM errors

Fig. 8 Coefficients of the improved deformation model estimated by (17)

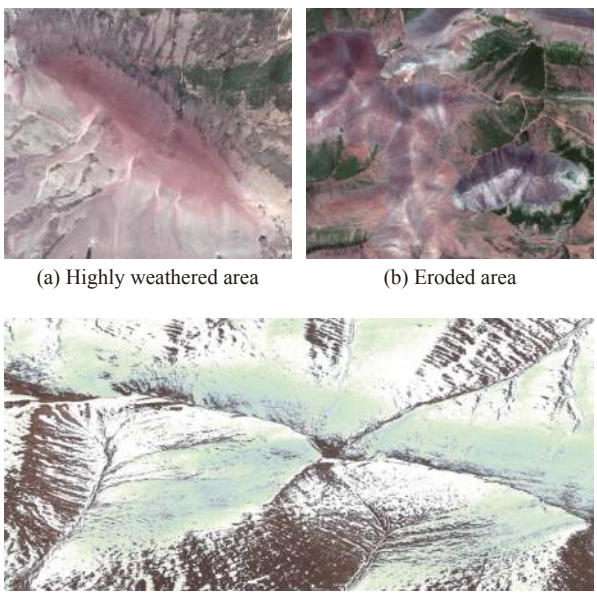

(a) Highly weathered area (b) Eroded area

(c) Ridge area

Fig. 9 High-resolution optical images of the three significant deformation areas of Fig. 8

4.3 Analysis of the surface deformation

The deformation between January 17, 2007 and October 28, 2007 shows a subsidence trend as in Fig. 10 where the red star in the last panel marks the location of leveling data (nearby the Beiluhe basin) used for validating the SBAS results. In the Fenghuoshan Mountain basin, some lower and flat areas free of artificial activities, have frozen soils experiencing thawing and heaving alternatively. The seasonal deformation has an opposite trend with that of the mean temperature (Fig. 2). In general, the soil is frozen in the cold season from October to the following March. When the temperature drops from October, the active layer has more heat release than absorption, resulting in the active layer freezing from both the top downward and from the bottom upward. The water freezes in the soil, so the frost heave appears. In the warm season from April to September, with the temperature rising, heat absorption in the soil surpasses the release. The active layer thaws downward as the heat transfers downward. The monthly mean temperature reaches the maximum in July and August, so the maximum thaw subsidence appeared on July 20, 2007 and July 22, 2008 (Fig. 10).

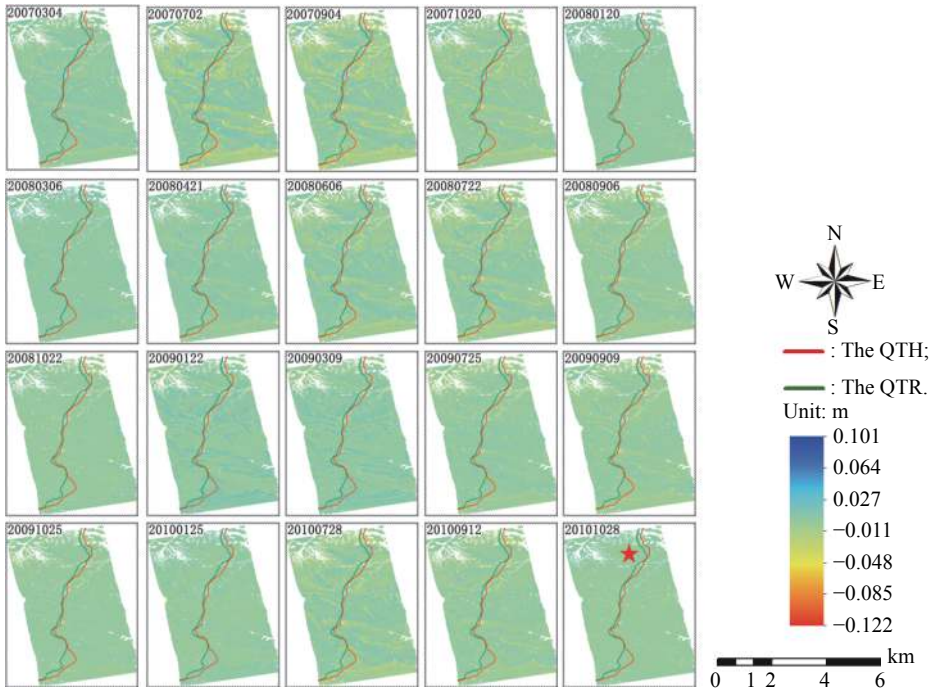

Fig. 10 Time series deformation of the study area relative to the InSAR image obtained on January 17, 2007

In the southwest of the Fenghuoshan Mountains, the active layer on the slope has more remarkable changes. The ridge usually has large subsidence, because a great amount of snow there melts when temperature rises. In the middle section of slopes, mainly consisting of Quaternary slope deposit soil that has low moisture content and vegetation coverage, there is little permafrost and small deformations. In the northeastern region, i.e., the Beiluhe basin, the permafrost shows great cyclical deformation. Several rivers passing through there bring moistures, which allows the permafrost to develop fully and the active layer to grow thick, causing large deformations [13]. The permafrost around the QTH and QTR has great subsidence, because the engineer activities altered the heat exchange and destroyed the water-energy balance between the frozen soil and the atmosphere.

For detailed studies, the deformation time series of the three typical points of Fig.1 are extracted and illustrated in Fig.11.

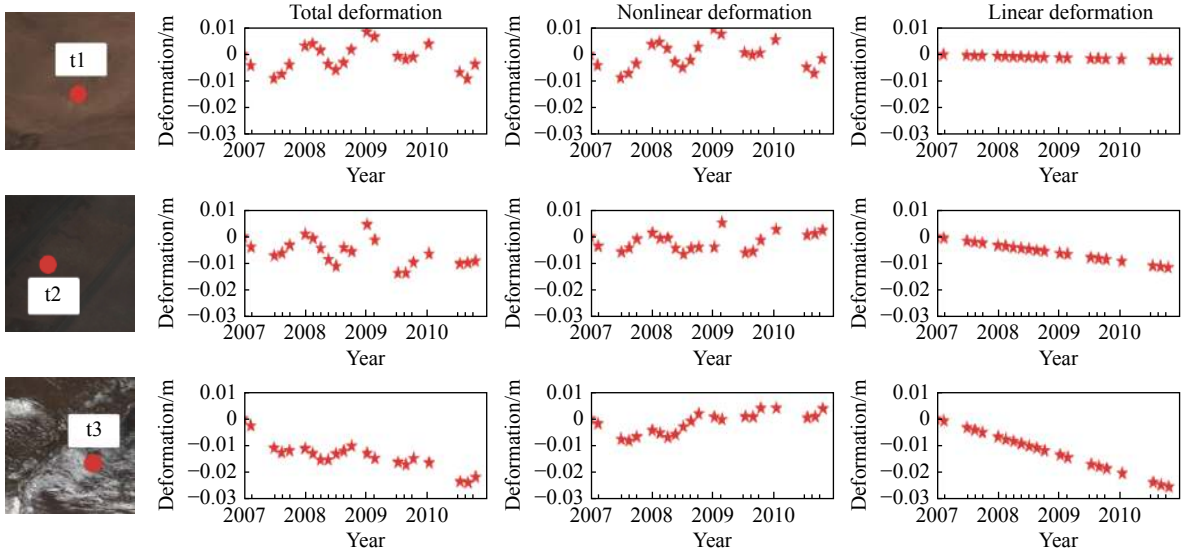

Fig. 11 Time series deformation of three typical feature points from 2007 to 2010

These three points distribute in the flat frozen soil area (t1), along the QTR (t2) and on a mountain ridge (t3), respectively (Fig. 1). Deformations over the three points all show seasonal patterns, but with different features. Point t1 is located in a flat region far away from the engineering area, so the active layer change is mainly affected by the temperature. The annual deformation there is 5 mm to 11 mm. Point t2 is close to the QTR, so human activities lead to continuous melting of the frozen soil, resulting in a large linear settlement (12 mm). Point t3 is located on a snow-covered mountain ridge, where the deformation is mainly due to snow surface elevation changes. The temperature rise and snow thaw cause great subsidence there. To sum up, permafrost deformation can be caused by temperature, topography and human activities.

4.4 Validation

We use the residual deformation, i.e., the un-modeled deformation, to verify the proposed SBAS-InSAR deformation model. Assuming that the InSAR observation errors have been properly removed, the root mean squares error (RMSE) of the residual deformation can reflect the accuracy of the deformation measurements. As shown in Fig. 12, the RMSE is randomly distributed around 0 with small dispersion. Points with large RMSEs are few, and the maximum value is 2 cm. Thus the proposed deformation model of the ICSBAS is feasible.

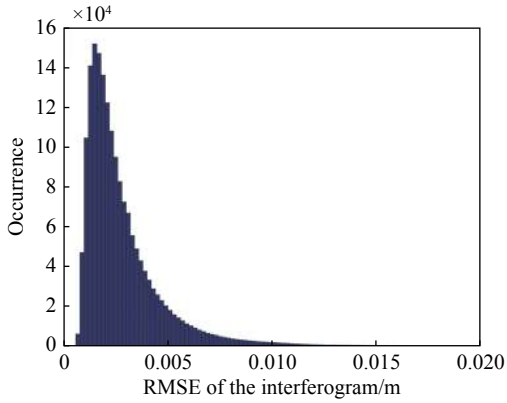

Fig. 12 RMSE of the interferogram residual

To assess the accuracy of the InSAR-derived results, we compare them with the leveling data (from January 2007 to December 2010 with one month interval) of an area close to the Beiluhe basin (marked by the red star in Fig. 10). To minimize the location difference, we select high coherent points by the nearest neighbor comparison referring to the leveling benchmark. Time series between them are illustrated in Fig. 13. The results show a consistent motion trend during the overlap observation time. The average motion rate of high coherence points is −4.5 mm/yr, similar to that of the leveling data −3.8 mm/yr. Furthermore, the leveling data and InSAR results show a similar nonlinear deformation trend of the seasonal frost heave and thawing subsidence of the active layer. However, the results have an absolute difference of 0.5−2 mm/yr. The observed discrepancies are probably caused by the spatial-temporal difference of the two data and the leveling observation error together with the ICSBAS data precision.

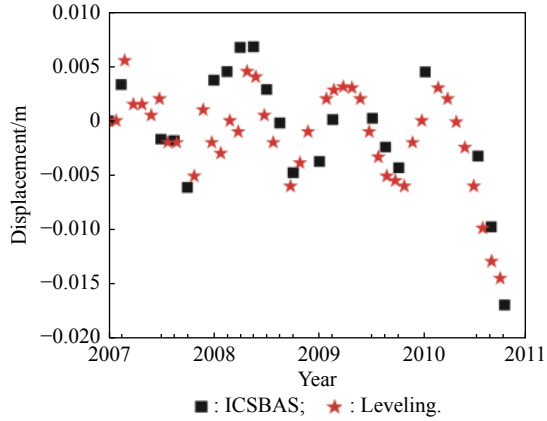

Fig. 13 Time series comparison between ICSBAS results and leveling data

5. Discussions

The permafrost in the middle and low latitudes of the QTP affects the local ecology and engineering projects, since it is sensitive to the thermal perturbation. This problem challenges the construction and operation of the QTR. As analyzed in previous sections, permafrost is mainly affected by topography, human activities and temperature. And the changes of the two former factors will inevitably lead to the change of temperature and moisture. Temperature changes will directly affect the permafrost environment.

5.1 Correlation between the temperature and permafrost deformation

The frozen soil has unique hydrothermal properties and is sensitive to the climate change. To investigate the influence of temperature on the ground surface deformation in frozen soil areas, we analyze the correlation between the time series deformation and the temperature. The results show that, the correlation coefficient between them ranges from −0.8 to 0.8 (Fig. 14). Temperature variations make the water in the frozen soil change between ice and water, showing surface subsidence or uplift. In addition, the temperature and deformation are negatively corre-

lated, with the coefficient of −0.6. However, if human activities and natural environmental factors have greater influence on permafrost deformation than the temperature, the deformation and temperature will have a positive correlation. And the relationship between them is relatively discrete and with no single peak.

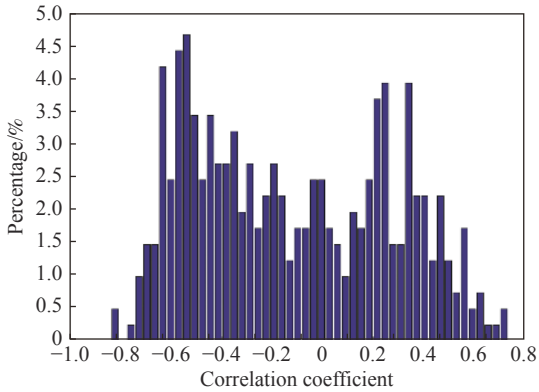

Fig. 14 Correlation analysis between deformation and temperature

5.2 Influence of human activities on permafrost deformation

The climate change has long but slow influence on the permafrost in the QTEC, but human engineering activities have short and fast influence. These two together generate the coupling superposition effect of the fast and slow process on the permafrost of subgrade [39,40]. Human engineering activities in the QTEC are always the most important influencing factors. We quantify these influences by the proportional variation of the positive and negative correlations between the deformation and temperature. According to the results, we divide the QTEC into the engineering damaged zone, transition zone and natural permafrost (Fig. 15). The blue and red dots represent the positive and negative correlations between the deformation and the temperature, respectively. The green, crimson and white bands represent the frozen areas that are 100 m, 500 m and 1 000 m away from the QTR, respectively. The stars are the three typical feature points.

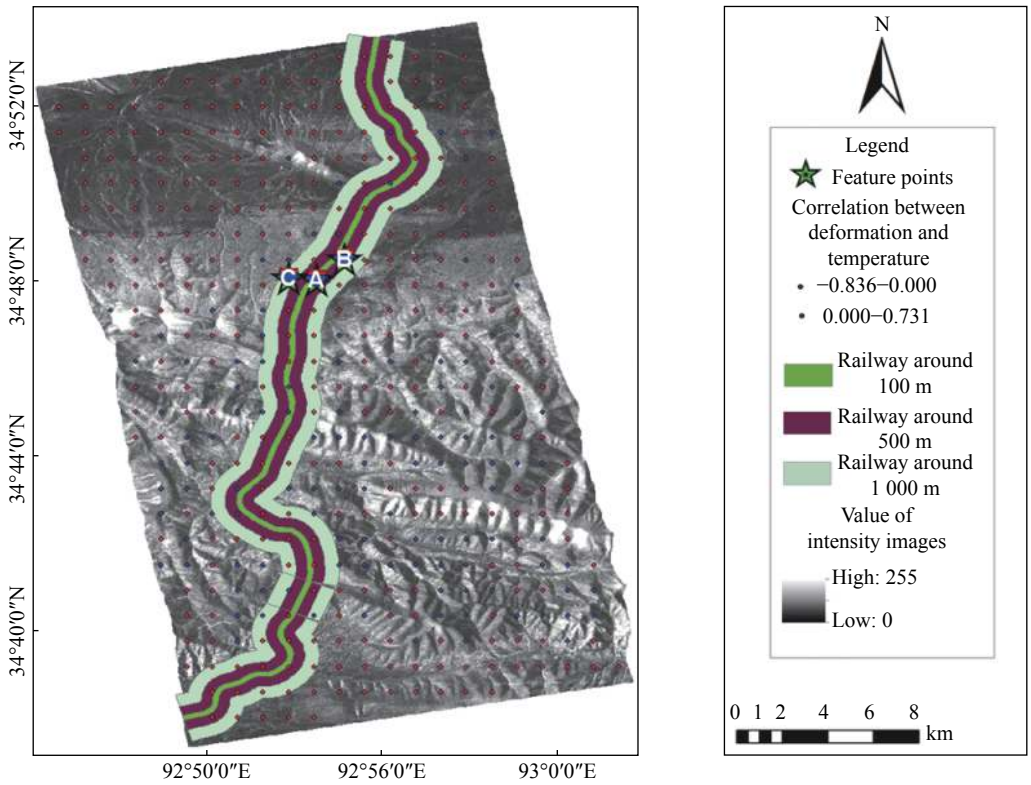

Fig. 15 Resampling of temperature and deformation

As shown in Fig. 15, blue dots are densely distributed in the green area, because a lot of major engineering activities are conducted there, such as the QTR, QTH, communication cable, oil pipeline, station building and residential facilities. Excavation and filling of the ground in these activities have changed the heat exchange conditions of the frozen soil and break the thermal balance of the active layer [41−43]. Moreover, the train load and these engineering activities also cause significant subsidence there. This changes the negative correlation between permafrost deformation and temperature, resulting in a large positive correlation ratio of 62.5%, much larger than the negative correlation ratio of 37.5% (Table 2), so we define the area as the engineering damaged zone.

Destruction to the permafrost environment due to human engineering activities gradually weakens with the growing distance to the QTR. Therefore, blue dots in the crimson area are sparse, accounting for only 20% of the total. This area is defined as the transition zone. There are very few blue dots in the white area, because it is far from the center of human engineering activities. However, the environmental factors such as topography and geomorphology, which will be analyzed in the following two sections, also contribute to the positive correlation ratio (7.5%). We define this area as the natural permafrost.

Table 2 Correlation ratio between temperature and deformation in the area with different distances from the QTR

Distance from the QTR	Positive correlation ratio/%	Negative correlation ratio/%
Within 100 m	62.5	37.5
100−500 m	20	80
Larger than 1 000 m	7.5	92.5

To investigate the influence of human engineering activities on the permafrost deformation, we analyze the correlation between time series deformation and temperature of the three typical points in Fig. 15 (points A, B and C), which are located in areas with a distance of 100 m, 500 m, and 1 000 m from the QTR, respectively (Fig. 16). r is the correlation coefficient between temperature and deformation. At point A, the influence of human engineering activities are far greater than the effect of temperature on the surface deformation, so the surface does not show seasonal shift between uplift and subsidence, but has a strong positive correlation with the temperature (0.48). With the gradual decrease of human engineering activities, temperature's influences increase. It can be seen from Fig.16 that the temperature and deformation are weakly negatively correlated at point B (−0.04). At point C, the surface deformation is hardly affected by human engineering activities. The correlation between deformation and temperature is $r = -0.6$.

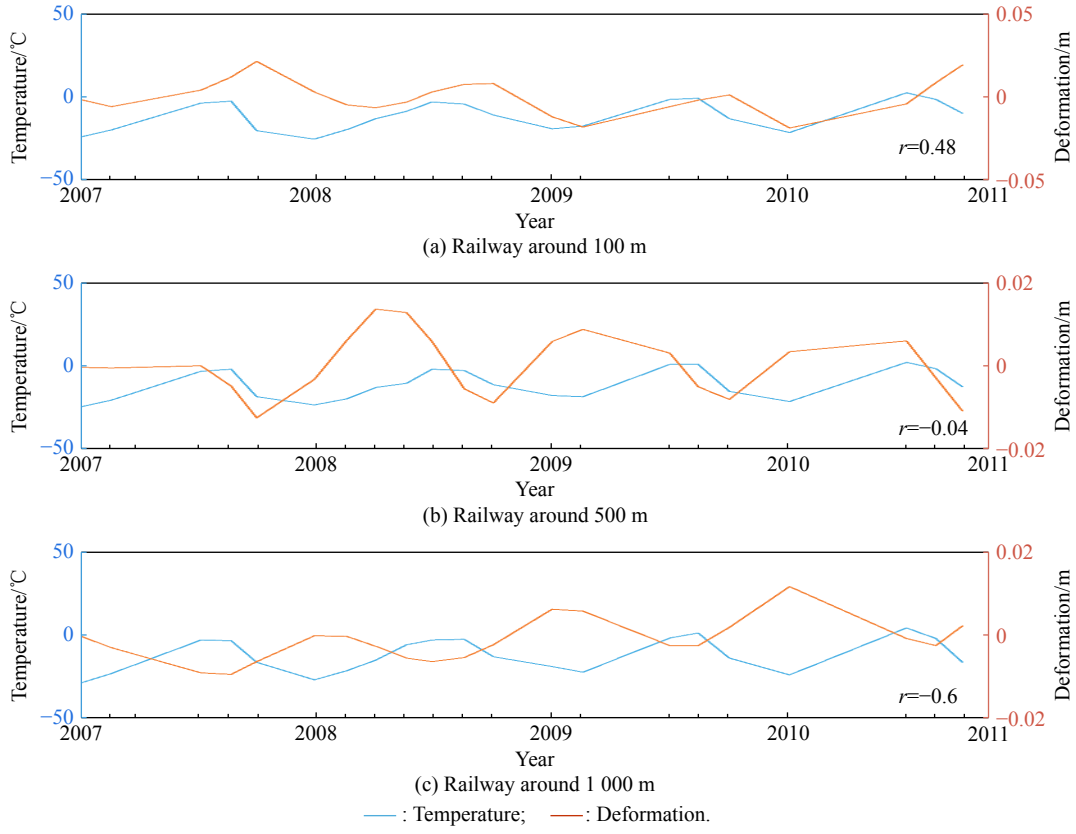

Fig. 16 Correlation between temperature and deformation over the three points (marked by A, B and C, respectively, in Fig. 15) in the areas with a distance of 100 m, 500 m and 1 000 m from the QTR

5.3 Influence of slope on permafrost deformation

We generate a slope map (Fig. 17) to study the relationship between slope and surface deformation of the frozen soil. The black solid rectangular present a flat permafrost region, and the black dotted rectangular is an area with

fluctuate permafrost. The blue and red dots represent the positive and negative correlations between the deformation and the temperature, respectively. The green, crimson and white bands represent the frozen areas that are 100 m, 500 m and 1 000 m away from the QTR, respectively. The stars are the three typical feature points. There is a significant negative correlation between the deformation and temperature in the flat area of the northern Fenghuoshan Mountains (the solid black rectangle in Fig. 17), in which the red dots (negative correlations points) account for 90.67% (Table 3). The permafrost in this area is mainly affected by temperature. With the seasonal temperature changing, the active layer experiences melting, freezing, cooling and warming yearly.

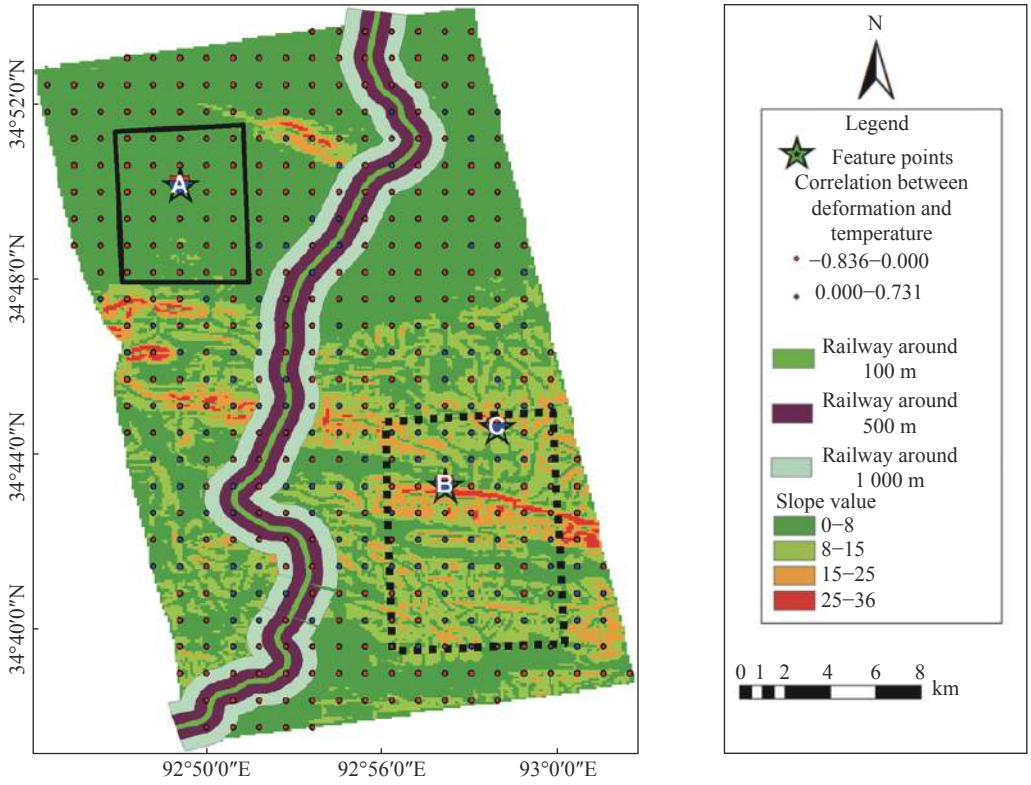

Fig. 17 Slope map of the study area

Table 3 Correlation ratio between the temperature and deformation with different slopes

Slope	Positive correlation ratio/%	Negative correlation ratio/%
0−8	9.33	90.67
8−36	38.1	61.9

The area south to the Fenghuoshan Mountains (the black dashed rectangle in Fig. 17) has diverse terrains and large altitude, so the correlation between the deformation and temperature is complicated (blue dot and red dot mix with each other). The positive and negative correlation coefficients of this area are 38.1% and 61.9%, respectively (Table 3). Permafrost is vertically distributed in this area [1]. In the upper part of the hillside (slope greater than 15°), positive correlation points are more than negative ones. Because little water comes from under the frozen layer and no recharge from the surface water, the soil of the upper part of the hillside is only recharged by the precipitation and the higher slope undercurrent. Therefore, the water supply is relatively insufficient and unstable. The insufficient soil moisture causes the underdeveloped frozen soil. In addition, due to the loss of snowmelt and fine-grained material, the slope surface has a low vegetation coverage, thus seriously impeding the development of the frozen soil. In the lower part (slope between 8° to 15°), positive and negative correlation points are randomly distributed. In these areas, water supply is contributed by the rising river, the melting and penetrating freezing layer and the deep undercurrent from the upper slope. These supply sources ensure a stable high water level, resulting in fully developed permafrost with thick active layers. The slope foot has fine sediments, thick soil, slow slope, and good water conditions. Thus there are swamps or ponds in the warm season, and ice piton, ice knoll in the cold season, which strongly affects the thermal stability.

In order to better illustrate the influence of slope on the permafrost deformation, we analyze the correlation between the deformation and temperature over three points (A, B and C in Fig. 17) located in the flat permafrost area, the upper part of the hillside, and the lower part of the hillside (Fig. 18). r is the correlation coefficient between temperature and deformation. Point A is negatively correlated with temperature, because the permafrost develops well in the flat area. In spring and summer, the frozen soil melts and the surface subsidence occurs. The maximum subsidence appears in September. In autumn and winter, with the soil freezes and uplifts. The maximum frost heave occurs in March. The deformation of point A coincides with the seasonal variation of permafrost, and the correlation coefficient is −0.52. Point B is in the upper part of the hillside, where the internal heat transfer and soil water content change are not active, because of the relatively lower temperature. In addition, the snow there works as a heat preservation layer, so the hydrothermal nature of the permafrost is relatively stable and the deformation is small. Point B is located on steep bare bedrock slope with coarse particles, so its deformation is mainly related to the material, with a strong positive deformation-temperature correlation (0.48). Point C is at the lower part of the hillside with thick sediments, small particles and wet soil. Thus the active layer is thicker and forms swamps or ponds in the warm seasons, and ice pitons or ice knolls in the cold season. This strongly affects the thermal stability of the frozen soil, resulting in large but irregular deformations.

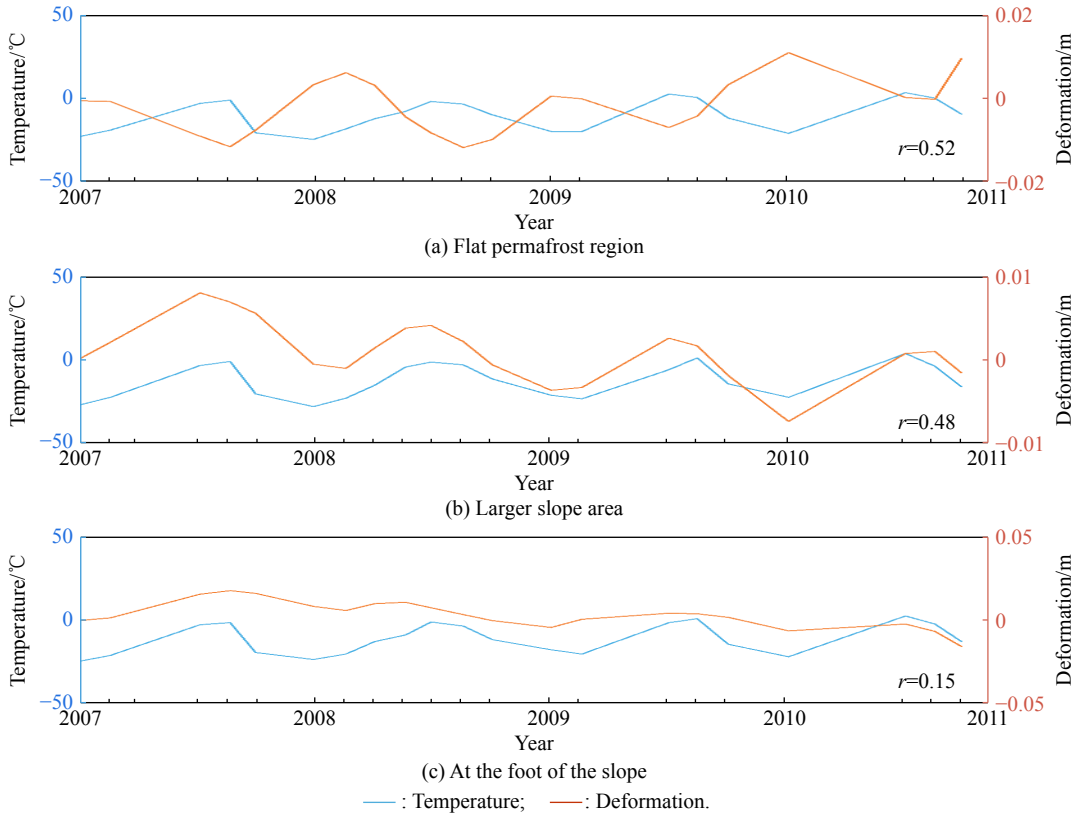

Fig. 18 Correlation between temperature and deformation over the three points (marked by A, B and C, respectively, in Fig. 17) located in the flat permafrost area, the upper part of the hillside, and the lower part of the hillside

5.4 Influence of aspect on permafrost deformation

Aspect determines the received sunlight and redistributes the solar radiation energy over the local surface, so it directly forms different climates in the local areas. Different solar radiation and surface turbulence contribute to different heat exchange conditions between the surface and atmosphere in the shady and sunny slopes [44]. Thus the thaw melting and frost heave on the two sides are different. In the Fenghuoshan Mountains, the shady and sunny slopes have an average annual temperature difference of 1.7−2.4℃, frozen soil thickness difference of 50−70 m, and significantly different development of underground ice [1]. Therefore, it is of great significance to

study the influence of aspect on the thermal condition of permafrost and for the analysis of permafrost environment. The study area is divided into shady slopes, half shady slopes, sunny slopes and half sunny slopes according to the terrain and sunshine conditions (Fig. 19).

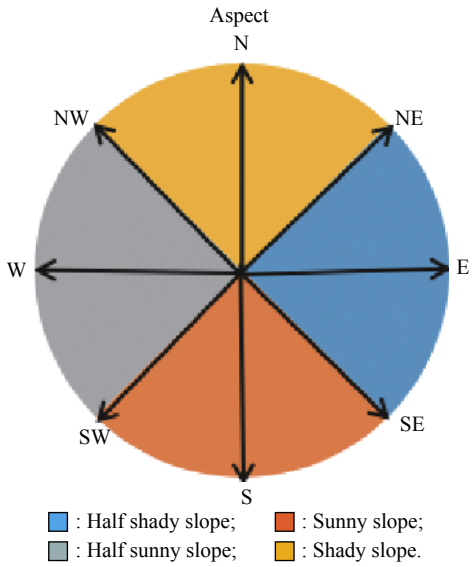

Fig. 19 Aspect

As shown in Fig. 20, the shady slope and sunny slope dominate the study area, so we focus on their influence on the frozen soil deformation. We also use the correlation points (blue and red points in the figure) to analyze the influence of aspect on the surface deformation. As shown in Table 4, in the sunny slope, positive correlation points account for 34.3%, much larger than that of the shady slope (19%), indicating that the impact of sunny slopes on permafrost is greater than that of shady slopes. The reason could be that different aspects result in different solar radiation, leading to the temperature difference that affects the permafrost. In the summer, with high solar altitude angle, both the shady and sunny slopes can receive solar radiation, so the temperature difference is small. The permafrost of shady and sunny slope melts with the increase of temperature, and melting degrees are similar because of the similar temperature. However, in the winter, the solar altitude angle is small, so the sunny slope can receive solar radiation for a long time, but the shady slope almost receives no solar radiation, resulting in great temperature difference [45]. Thus, the frost heave is small in the sunny slope, but big in the shady one. Therefore, the frozen soil of the shady slope is more stable and less affected by the aspect.

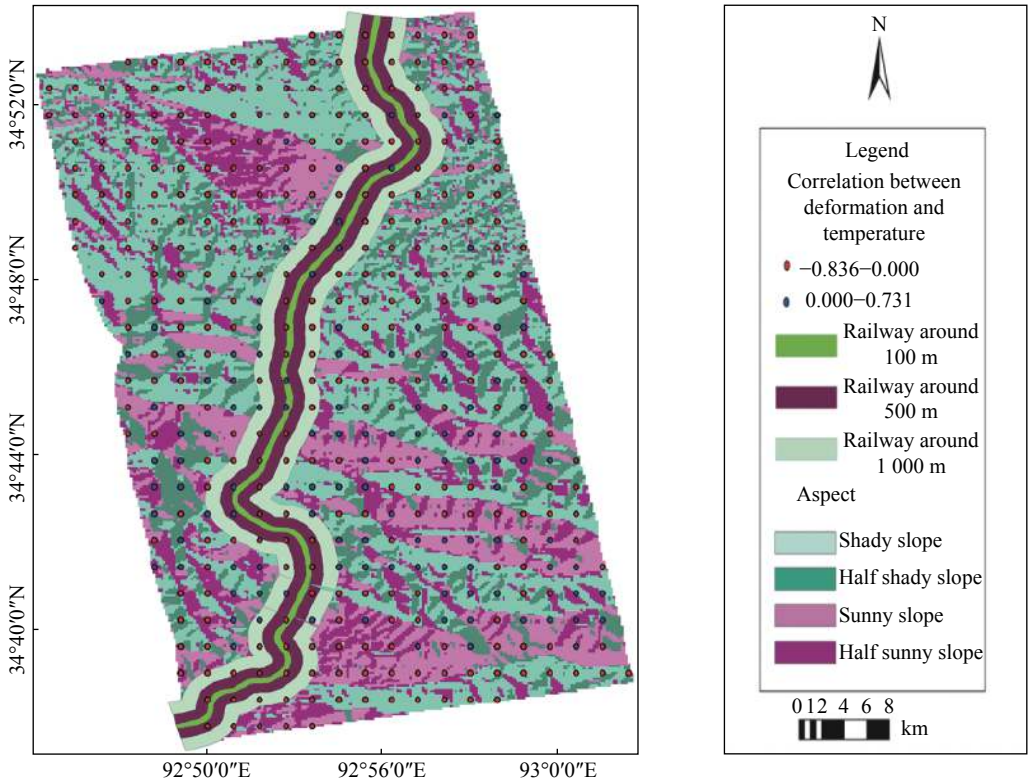

Fig. 20 Aspect map of study area

Table 4 Correlation ratio between the temperature and deformation of different aspects

%

Slope	Positive correlation ratio	Negative correlation ratio
Shady slope	19	81
Sunny slope	34.3	65.7

6. Conclusions

This paper proposes the ICSBAS technology. This method improves the coherent point density and enhance the interpretability of the deformation results, by identifying intermittent coherent points. And by filtering the atmospheric delay phase using a periodic function, it improves the monitoring accuracy.

We adopt the ICSBAS method to estimate the surface deformation over the permafrost area of the Fenghuoshan Mountains section, Qinghai-Tibet Plateau. The results show that the active layer of the natural permafrost region has frost heave and thaw settlement (4.7 cm to 8.4 cm) alternatively, while the maximum settlement along the QTR reaches 12 cm. These results agree with the leveling data in displacement rates as well as time series.

We find that the permafrost deformation is correlated with temperature, human activities and topography. The surface deformation of the natural frozen soil area is negatively correlated with the temperature, and the correlation coefficients mainly concentrate on −0.6. Other regions have both negative and positive correlations with temperature, due to the influence of human activities and topography. The QTEC along the QTR is divided into the engineering damaged zone, transition zone and natural permafrost, based on the interfering degree of human engineering activities on the permafrost environment. The influence of slope and aspect on the development of permafrost is also analyzed qualitatively to obtain the spatial and temporal distribution law of the permafrost deformation.

However, some problems need further study. First, this study does not quantify the influence of human activities and environmental factors on the deformation of frozen soil. Second, this study uses single track InSAR data, not able to monitor deformations in both the horizontal and vertical directions. Using multiple satellite data could enhance the reliability of the results.

References

[1] ZHOU Y W, GUO D X. Principle characteristics of permafrost in China. Journal of Glaciology and Geocryology, 1982, 4(1): 1–19. (in Chinese)

[2] NELSON F E, ANISIMOV O A, SHIKLOMANOV N I. Subsidence risk from thawing permafrost. Nature, 2001, 410(6831): 889–890.

[3] SMITH S, BURGESS M, RISEBOROUGH D, et al. Recent trends from Canadian permafrost thermal monitoring network sites. Permafrost and Periglacial Process, 2005, 16: 19–30.

[4] YU Q H, LIU Y Z, TONG C J, et al. Analysis of the subgrade deformation of the Qinghai-Tibetan Highway. Journal of Glaciology and Geocryology, 2002, 24(5): 623–627. (in Chinese)

[5] JONATHON D L, HEATH S, MICHAEL T, et al. Application of differential global positioning systems to monitor frost heave and thaw settlement in tundra environments. Permafrost and Periglacial Processes, 2003, 14: 349–357.

[6] SCOTT W, SELLMANN P, HUNTER J. Geophysics in the study of permafrost. Geophysicists Investigation in Geophysics, 1990, 5: 355–384.

[7] HINKEL K, DOOLITTLE J, BOCKHEIM J, et al. Detection of subsurface permafrost features with ground-penetrating radar, barrow, alaska. Permafrost Periglacial Process, 2001, 12: 179–190.

[8] MASSONNE D, ROSSI M, CARMONA C, et al. The displacement field of the landers earthquake mapped by radar interferometry. Nature, 1993, 364(6433): 138–142.

[9] WANG Z, LI S. Detection of winter frost heaving of the active layer of arctic permafrost using SAR differential interferograms. Proc. of the IEEE International Geoscience and Remote Sensing Symposium, 1999, 4: 1946–1948.

[10] LI Z, LI X W, LIU Y Z, et al. Detecting the displacement field of thaw settlement by means of SAR interferometry. Journal of Glaciology and Geocryology, 2004, 26(4): 389–396. (in Chinese)

[11] BUTTERWORTH C. Measuring seasonal permafrost deformation with differential interferometric synthetic aperture radar. Calgary, Canada: University of Calgary, 2008.

[12] XIE C, LI Z, LI X W. A study of deformation in permafrost regions of Qinghai-Tibet plateau based on ALOS/PALSAR D-InSAR interferometry. Remote Sensing for Land and Resources, 2008, 30(3): 15–19. (in Chinese)

[13] WANG P. Using D-InSAR to monitor the motion of frozen ground in Qinghai-Tibet Plateau. Changsha, China: Centrol South University, 2008. (in Chinese)

[14] HU B, WANG H S, JIA L L. DInSAR technology to monitor deformation of Qinghai-Tibet Plateau permafrost experimental study. Geodesy and Geodynamics, 2010, 30(5): 53–56.

[15] FERRETI A, PRATI C, ROCCA F. Non-linear subsidence rate estimation using permanent scatterers in differential SAR interferometry. IEEE Trans. on Geoscience and Remote Sensing, 2000, 38(5): 2202–2212.

[16] BERARDINO P, FORNARO G, LANARI R, et al. A new algorithm for surface deformation monitoring based on small baseline differential SAR interferograms. IEEE Trans. on Geoscience and Remote Sensing, 2002, 40(11): 2375–2383.

[17] LIU L, ZHANG T J, WAHR J et al. InSAR measurements of surface deformation over permafrost on the North Slope of Alaska. Journal of Geophysical Research Earth Surface, 2010, 115(F3). DOI: 10.1029/2009JF001547.

[18] SHORT N, BRISCO B, COUTURE N, et al. A comparison of TerraSAR-X, RADARSAT-2 and ALOS-PALSAR interferometry for monitoring permafrost environments, case study from Herschel Island, Canada. Remote Sensing of En-

vironment, 2011, 115(12): 3491–3506.
[19] CHEN F L, LIN H, LI Z, et al. Interaction between permafrost and infrastructure along the Qinghai-Tibet Railway detected via jointly analysis of C- and L-band small baseline SAR interferometry. Remote Sensing of Environment, 2012, 123: 532–540.
[20] LIU L, SCHAEFER K, ZHANG T J, et al. Estimating 1992 –2000 average active layer thickness on the Alaskan North Slope from remotely sensed surface subsidence. Journal of Geophysical Research Earth Surface, 2012, 117: 14.
[21] LI S S, LI Z W, HU J, et al. Investigation of the seasonal oscillation of the permafrost over Qinghai-Tibet Plateau with SBAS-InSAR algorithm. Chinese Journal of Geophysics, 2013, 56(5): 1476–1486. (in Chinese)
[22] LIU L, SCHAEFER K, GUSMEROLI A, et al. Seasonal thaw settlement at drained thermokarst lake basins, Arctic Alaska. The Cryosphere, 2014, 8(6): 5793–5822.
[23] SHORT N, LEBLANC A M, SLADEN W, et al. RADARSAT-2 D-InSAR for ground displacement in permafrost terrain, validation from Iqaluit Airport, Baffin Island, Canada. Remote Sensing of Environment, 2014, 141: 40–51.
[24] SCHAEFER K, LIU L, PARSEKIAN A, et al. Remotely sensed active layer thickness (ReSALT) at Barrow, Alaska using interferometric synthetic aperture radar. Remote Sensing, 2015, 7(4): 3735–3759.
[25] ZHAO R, LI Z W, FENG G C, et al. Monitoring surface deformation over permafrost with an improved SBAS-InSAR algorithm: with emphasis on climatic factors modeling. Remote Sensing of Environment, 2016, 184: 276–287.
[26] ZHANG Y H, WU H A, SUN G T. Deformation model of time series interferometric SAR techniques. Acta Geodaetica et Cartographica Sinica, 2012, 41(6): 864–869. (in Chinese)
[27] WANG C, ZHANG Z J, ZHANG H. Seasonal deformation features on Qinghai-Tibet railway observed using time-series InSAR technique with high-resolution TerraSAR-X images. Remote Sensing Letters, 2017, 8(1): 1–10.
[28] CHEN Y X, JIANG L M, LIANG L L, et al. Monitoring permafrost deformation in the upstream Heihe River, Qilian Mountain by using multi temporal Sentinel INSAR dataset. Chinese Journal of Geophysics, 2019, 62(7): 2441–2454. (in Chinese)
[29] HUANG S B, CHANG Z Q, XIE C. Deformation monitoring of frozen soil in salt lake area based on SBAS-InSAR. Advances in Geosciences, 2020, 10(2): 100–120.
[30] CHENG J, WANG T, ZHU Z R, et al. Research on subgrade defects of Fenghuoshan section on Qinghai-Tibet railway and countermeasures. Railway Standard Design, 2015, 8(59): 14–17. (in Chinese)
[31] COLESANTI C, FERRETTI A, NOVALI F, et al. SAR monitoring of progressive and seasonal ground deformation using the permanent scatterers technique. IEEE Trans. on Geoscience and Remote Sensing, 2003, 41(7): 1685–1701.
[32] KAMPES B M, HANSEEN R F. Ambiguity resolution for permanent scatterer interferometry. IEEE Trans. on Geoscience and Remote Sensing, 2004, 42(11): 2446–2453.
[33] YANG H L, PENG J H, WANG B C, et al. Ground deformation monitoring of Zhengzhou city from 2012 to 2013 using an improved IPTA. Natural Hazards, 2016, 80: 1–17.
[34] SCHMID T, DAVID A. Time-dependent land uplift and subsidence in the Santa Clara Valley, California. Journal of Geophysical Research Solid Earth, 2003, 108(B9): 2416.
[35] BROWN C G, SARABANDI K, PIERCE L E. Validation of the shuttle radar topography mission height data. IEEE Trans. on Geoscience and Remote Sensing, 2005, 43(8): 1707–1715.
[36] LI Z W, DING X L, HUANG C, et al. Improved filtering parameter determination for the Goldstein radar interferogram filter. ISPRS Journal of Photogrammetry and Remote Sensing, 2008, 63(6): 621–634.
[37] COSTANTINI M, ROSEN P. A generalized phase unwrapping approach for sparse data. Proc. of the IEEE International Geoscience & Remote Sensing Symposium, 1999, 1(10): 267–269.
[38] GARBALLO G F, FIEGUTH P W. Probabilistic cost functions for network flow phase unwrapping. IEEE Trans. on Geoscience and Remote Sensing, 2001, 38(5): 2192–2201.
[39] ZHANG L X. Regularity of ground temperature variation in Qinhgai-Tibet Plateau permafrost region and its effect on subgrade stability. China Railway Science, 2000, 21(1): 37–47.
[40] YUAN S C, ZHANG L X, HAN L M, et al. Influences of environmental conditions on construction safety reliability of Qinghai-Tibet railway in permafrost region. Journal of Engineering Geology, 2006, 14(4): 433–437.
[41] DONG C H, ZHAO X Q. Analysis on subgrade deformation features and influence factors in permafrost regions on Qinghai-Tibet Railway. Railway Standard Design, 2013, 6: 5–8. (in Chinese)
[42] YANG X D. The study of the subgrade deformation and characteristic over permafrost. Shaanxi, China: Xi'an Jiaotong University, 1996.
[43] WU Q B, ZHU Y L, SHI B. Study of frozen soil environment relating to engineering activities. Journal of Glaciology and Geocryology, 2001, 23(2): 200–207.
[44] SUN Z, WANG L, BAI M, et al. Finite element analysis on temperature field of Qinghai-Tibet Railway embankment on permafrost. Chinese Journal of Rock Mechanics and Engineering, 2004, 23(20): 3454–3459. (in Chinese)
[45] CHOU Y L, SHENG Y, MA W, et al. Calculation of difference in temperature between sunny slope and shady slope along railways in permafrost regions in Qinghai-Tibet plateau. Chinese Journal of Rock Mechanics and Engineering, 2007, 26(2): 4102–4107. (in Chinese)

Biographies

YANG Honglei was born in 1983. He is a Ph.D. and an associate professor in China University of Geosciences (Beijing). His research interests include deformation monitoring using interferometric synthetic aperture radar interferomet (InSAR) time series and remote sensing data processing.
E-mail: hongleiyang@cugb.edu.cn

JIANG Qiao was born in 1994. He graduated from China University of Geosciences with a master's degree. He is an engineer of Central Southern China Electric Power Design Institute Co., Ltd. His current research interests are development of GPS and interferometric synthetic aperture radar algorithms, and studies of structural and ground deformations.
E-mail: 2640105418@qq.com

HAN Jianfeng was born in 1996. He is a graduate student in China University of Geosciences (Beijing). His research interest is interferometric synthetic aperture radar.
E-mail: 924247310@qq.com

KANG Ki-Yeob was born in 1987. He received his bachelor's and master's degrees in naval architecture and ocean engineering, in 2012 and 2014, from Pusan National University in South Korea and Ph.D. degree in construction management from Curtin University in Perth, Australia in March 2020. His research interests are oil and gas energy resources, offshore drilling technologies, construction materials, engineering design, and facility management.
E-mail: kiyeob.kang@postgrad.curtin.edu.au

PENG Junhuan was born in 1964. He received his Ph.D. degree in geodesy from Wuhan University, Wuhan, China, in 2003. He is a professor with the School of Land Science and Technology, China University of Geosciences, Beijing, China. His current research interests are in the areas of temporal-spatial data analysis, surveying adjustment, applied statistics, and their associated application in surveying engineering, image geodesy, remote sensing, and satellite geodesy.
E-mail: pengjunhuan@163.com